Atacama Clear for Complex 3D Imaging of Organs

Neranjan de Silva*[1], Lauretta A. Lacko*[2, 3], Edgar A. Jamies[4], Todd Evans[1,5+] and Romulo Hurtado[1+]

1) Department of Surgery, Weill Cornell Medicine, New York, NY, USA

2) Department of Medicine, Weill Cornell Medicine, New York, NY, USA

3) Human Therapeutic Organoid Core Facility, Weill Cornell Medicine, New York, NY USA

4) Department of Medicine, Memorial Sloan Kettering Cancer Center, New York, NY, USA

5) Weill Cornell Center for Genomic Health

*These authors contributed equally

[+]Corresponding Authors

Corresponding Author Lead Contact:

Romulo Hurtado, Ph.D.

Assistant Professor of Cell and Developmental Biology Research

Department of Surgery

Weill Medical College of Cornell University

1300 York Avenue

New York, NY 10021

*Correspondence: roh2002@med.cornell.edu

Abstract

3D reconstructive imaging is a powerful strategy to interrogate the global architecture of tissues. We developed Atacama Clear (ATC), a novel method that increases 3D imaging signal-to-noise ratios (SNRs) while simultaneously increasing the capacity of tissue to be cleared. ATC potentiated the clearing capacity of all tested chemical reagents currently used for optical clearing by an average of 68%, and more than doubled SNRs. This increased imaging efficacy enabled multiplex interrogation of tough fibrous tissue and specimens that naturally exhibit high levels of background noise, including the heart, kidney, and human biopsies. Indeed, ATC facilitated visualization of previously undocumented adjacent nephron segments that exhibit notoriously high autofluorescence, elements of the cardiac conduction system, and the distinct human glomerular tissue layers, at single cell resolution. Moreover, ATC was validated to be compatible with fluorescent reporter proteins in murine, zebrafish, and 3D stem cell model systems. These data establish ATC for 3D imaging studies of challenging tissue types.

INTRODUCTION

Understanding the global architecture of cellular tissue compartments provides key insight into normal and pathological organ physiology. However, visualizing the 3-dimensional (3D) organization of tissue is limited by its natural opacity that causes light scattering and prevents deep penetration of light. Traditionally, these challenges have been addressed by assaying serial thin histological sections, and then attempting to derive 3D information. This approach, however, is laborious and time consuming, and can result in unsatisfactory reconstruction in the case of damaged or lost sections. To this end, our understanding of systems-level organ structure has been greatly advanced by optical clearing methods that enable direct 3D imaging through intact organs [1,2].

In general, optical clearing methodologies consist of a lipid removal step that makes the whole tissue accessible, and a step immersing the tissue in a solution that matches the refractive index of the specimen to allow light to travel through the sample unimpeded by light scatter. These protocols can be broadly categorized into solvent-based and aqueous-based protocols [1,2]. Of these, aqueous methods are advantageous because they maintain the natural state of tissue and preserve antigens and fluorescent reporters that can be lost using hydrophobic solvents and alcohols. Indeed, aqueous and hyperhydration methods such as SCALE [3,4], ClearT[2] [5], SeeDB [6], FRUIT [7], and CUBIC [8-10] are among those most widely used because they are simple, generally non-toxic, compatible with *in vivo* tracers, and can preserve fluorescent reporters.

Tissue types vary on how amenable they are to optical clearing and 3D imaging. For instance, tough fibrous tissue, such as muscles, are very difficult to optically clear. Moreover, the autofluorescence naturally exhibited by tissue remains a major challenge in 3D imaging, as it limits the ability to detect signals from fluorescently labeled structures [1]. This presents difficulties for multiplex 3D imaging of organs such as the kidney that exhibits notoriously high background noise, or the heart that is both fibrous and has significant autofluorescence. Indeed, interrogating human biopsies of such organs are markedly challenging as they are tougher and exhibit even higher autofluorescence than counterpart specimens from commonly used small mammalian animal models.

Here, we developed Atacama Clear (named for the clear skies of the Atacama Desert), an aqueous optical clearing protocol designed specifically to address the difficulties associated with imaging tough fibrous tissues and high background autofluorescence. We demonstrate that Atacama Clear (ATC) potentiates the optical clearing capacity of all currently used optical clearing chemicals that were tested (eight in total). Moreover, we demonstrate that ATC can mitigate tissue autofluorescence, and consequently significantly improves signal-to-noise ratios (SNRs). ATC was proven to be compatible with fluorescent reporters in zebrafish, murine, and 3D stem cell models. The advantageous properties of ATC readily facilitated 3D imaging of the cardiac conduction system of the murine heart [11], as well as the gross intact structure of adjacent renal connecting and distal convoluted tubule nephron segments that had previously remained undocumented [12,13]. Moreover, ATC enabled multiplex 3D imaging of distinct glomerular tissue layers in human kidney biopsies, with cellular resolution [14].

RESULTS

Optimization of optical clearing protocols

Numerous valuable optical clearing protocols have been developed over the last several years [1,2]. To the best of our knowledge, however, an aqueous technique has yet to be optimized for imaging studies that are challenged due to inherently high degrees of background noise. Indeed, as can be seen in Figure 1A, the kidney and heart exhibit relatively high levels of autofluorescence (green autofluorescence of kidney, heart and spleen imaged in the same field of view). We sought to maximize signal-to-noise ratios in optical clearing studies, particularly for organs such as the kidney that exhibit high background autofluorescence, and those such as the heart that exhibit significant autofluorescence and are among the most challenging tissue types to clear due to their robust cytoskeletal network.

Blood is a known deterrent of optical clearing and a main source of autofluorescence. This is readily illustrated, for instance, in perfused murine kidneys and hearts where regions of the organ with the most amount of blood exhibit the highest autofluorescence (Supplemental Fig. 1-D) and are the most resistant to optical clearing (Supplemental Fig. 1E, F). Thus, a blood removal method would be beneficial for mitigating background noise and augmenting optical clearing. As shown in these examples, however, perfusion is often variable and

incomplete. Notably, Hydrogen peroxide (H_2O_2) has been widely used to remove blood. However, it is well established that H_20_2 damages tissue as catalase converts H_2O_2 to water and oxygen, and the accumulation of oxygenation causes tissue tearing and autofluorescence of damaged tissue regions [15]. Indeed, tissue tearing was readily observed when heart or kidney sections were treated with standard H_2O_2 treatment (Supplemental Fig. G, H, arrow heads mark sites of tissue tearing, arrows mark oxygenation within tissue). Tissue regions damaged by H_2O_2 oxygenation exhibited increased autofluorescence, as demonstrated in kidney sections before and after treatment with standard H_2O_2 (Supplemental Fig. 1I, before treatment; 1J, after treatment, arrows point to regions of tissue damage that increased in autofluorescence).

To address this challenge, we aimed to develop an alternative method for blood removal. Since oxygenation corresponded with tissue damage and increased autofluorescence, we screened eight putative reversible inhibitors of catalase to moderate oxygen production while maintaining blood removal (Supplemental Fig. 1K). Sodium azide (NaN_3) used with H_2O_2, termed Atacama-H_2O_2 (AT-HP), precluded visible oxygenation (Supplemental Fig. 1K, effervescing observed in all other conditions, but not with NaN_3). In contrast to standard protocols, treatment of 1 mm heart sections and whole kidneys showed that AT-HP fully decolorized tissue without causing degradation (Supplemental Fig. 1L-Q). Critically, AT-HP reduced autofluorescence, as illustrated in kidneys divided into two equal halves, with one half left untreated and the second treated with AT-HP (Fig. 1B). AT-HP progressively diminished autofluorescence in a time dependent manner, resulting in a compelling difference in background noise between treated and untreated kidneys, which was also validated in 1 mm thick heart sections (Fig. 1B and C, treated and untreated kidney imaged in the same field of view; Supplemental Fig. 1R-T, time dependent decrease in autofluorescence of kidney halves; Supplemental Fig. 1U-W, time dependent decrease of autofluorescence in heart sections). Kidney sections treated with AT-HP for 24 hr exhibited an average 57% decrease in green autofluorescence (Fig. 1C and 1D, mean reduction in green autofluorescence = 57% ± 8.9%; 83% ± 1.9% reduction in red autofluorescence).

We further validated the high preservation of tissue integrity and diminished tissue autofluorescence using AT-HP. To this end, we compared Atacama imaging to CUBIC, which is regarded as among the leading decolorizing optical clearing methods that highly preserves tissue. To perform direct comparisons, adjacent

500 µm sections of an individual heart or kidney were each treated for 24 hours with CUBIC1 or AT-HP (Fig. 1E-J). AT-HP more efficaciously decolorized tissue (Fig 1E, H) and better preserved tissue morphology (Fig. 1F, I). Although sections were not torn by CUBIC1, they were enlarged and distorted in shape. By contrast, ATC sections maintained their flat morphology. Analyses of tissue background demonstrated that sections treated with AT-HP had on average 50% less autofluorescence than adjacent sections treated with CUBIC1 (Fig. 1G, J, autofluorescence of tissue sections imaged in the same field of view after treatment with CUBIC1 or AT-HP; and 1K, mean fluorescent intensity of autofluorescence, CUBIC = 76.07 ± 11.44, AT-HP = 38.5 ± 5.08; $p<0.0001$).

The decrease in autofluorescence and high preservation of tissue integrity suggested that superior immunofluorescence signals could be obtained using AT-HP. Indeed, due to the low background noise observed with AT-HP, we hypothesized that it would enable imaging with higher SNRs. To test this, adjacent kidney or heart sections were treated with CUBIC1 or AT-HP, and then immunostained together in the same receptacle (Fig. 1L-Q, arterial blood vessel staining, SMA, green). Imaging of sections side-by-side in the same field revealed robust immunofluorescent staining with significantly lower background noise in AT-HP treated sections, as compared to CUBIC (Fig. 1L, O). Differences in the contrast between vessel staining and surrounding tissue were readily evident in high magnification images (Fig 1M, N, kidney sections; P, Q, heart sections). Indeed, quantification of immunofluorescent staining and tissue background signals revealed that Atacama imaging provided a 57% greater signal-to-noise ratio (Fig. 1R, signal-to-noise ratio: CUBIC = 1.144 ± 0.06; AT-HP = 1.804 ± 0.39, $p<.0001$).

We next tested our hypothesis that decreased background noise facilitates multiplex imaging of challenging tissue types. Specifically, we assayed the kidney which is notoriously difficult to image due to its high autofluorescence, particularly in the green field, which limits the ability to simultaneously visualize different organ compartments by multiplex immunofluorescence (IF). Consequently, we chose to perform imaging of the different tissue layers of the glomerulus, which is furthermore demanding due to the high tissue preservation required to maintain the delicate architecture of this tissue [14]. As can be seen in Figure 1R-U and

Supplemental Movie 1, the podocytes (Podocalyxin, red), mesangium (Pdgfr-β, blue) and endothelium (Endomucin, green) of the glomerulus were readily distinguished using AT-HP [16,17].

Critically, we also discovered that AT-HP significantly augments optical clearing. Adjacent sections from non-perfused kidneys were left untreated or treated with AT-HP, and then both sections were immersed in optical clearing solutions from published 3D imaging techniques. Strikingly, we discovered that AT-HP increased the optical clearing capacity of all tested refractive index matching solutions (Fig. 2A), including Quadrol (CUBIC protocols), urea (Scale protocols) [4], formamide (ClearT^2 and RTF) [5], glycerol (Clarity) [18], fructose (SeeDB and Fruit) [6,7], sorbitol (sRIMS) [19], sucrose (UbasM) [20], and DMSO (FOCM) [21]. Treatment with AT-HP increased the optical clearing capacity of these reagents by an average 68% (Fig. 2B), as compared to untreated tissue sections. Taken together, these data establish that AT-HP mitigates autofluorescence, facilitates superior imaging by providing higher SNRs, and augments optical clearing of tissue.

To continue protocol development, we assayed the autofluorescence of samples upon treatment with optical clearing solutions. As mentioned above, aqueous hyperhydration methods are widely used because they are simple, non-toxic, and highly preserve antigens and fluorescent reporters that can be lost with the use of hydrophobic solvents and alcohols. ClearT^2 is an earlier method used to clear embryonic tissues, but lacks the capability to clear larger adult organs [5]. CUBIC, on the other hand, has been widely used for clearing all adult organs [8,9]. However, CUBIC utilizes high concentrations of detergents that has been reported to disrupt proteins and fluorescent reporters [22]. To this end, the MACS protocol was recently developed to optically clear adult organs, including muscle, without the drawback of using high levels of detergents [22]. Thus, we imaged the autofluorescence of adjacent kidney sections before and after treatment with formamide, quadrol, or m-Xylylenediamin (MXDA), active reagents utilized in ClearT^2, CUBIC, and MACS, respectively (Supplemental Fig. 2A-D). Treatment with formamide resulted in a decrease in autofluorescence (Supplemental Fig. 2A, representative images before and after treatment; Supplemental Fig. 2D, mean change in fluorescent intensity). By contrast, treatment with 20%, 40% or 50% MXDA increased kidney autofluorescence (Supplemental Fig. 2B, images before and after treatment; and Supplemental Fig. 2D). Moreover, 25% quadrol, 40% quadrol, and CUBIC 1 reagent (25% quadrol, 25% urea, and 15% triton-x) increased kidney

autofluorescence (Supplemental Fig. 2C, images before and after treatment; and Supplemental Fig. 2D). Putative increases in non-specific signal were reported in the development of CUBIC [8]. Based on these results, protocol development was continued using formamide. It was hypothesized that formamide combined with other refractive-indexed matched reagents would provide greater optical clearing capabilities. Glycerol was chosen for the following beneficial properties: a) it can clear tissue with a refractive index that closely matches biological tissues; b) it is hydrophilic, precluding the need for dehydration with hydrophobic solvents and alcohols that compromise membrane and fluorescent reporter protein integrity; c) it has excellent optical properties, including the preservation of fluorescence, and does not increase autofluorescence; and d) it is non-toxic, and simple to integrate. To test our hypothesis, we used murine heart sections due to their resistance to optical clearing. Non-perfused hearts were sectioned at varying thicknesses and then treated either with 25% formamide + 75% glycerol solution, which we termed Atacama optical clearing (AT-OC) solution, or ClearT^2 that is comprised of 50% formamide and 20% PEG (Supplemental Fig. 2E). ClearT^2 failed to clear heart sections thicker than 500 µm. By contrast, AT-OC readily cleared heart sections of 850 µm thickness and exhibited more than a 2-fold greater clearing capacity than ClearT2 (Supplemental Fig. 2F). Moreover, 1mm thick sections of perfused hearts that lacked blood were readily made transparent with AT-OC (Supplemental Fig. 2G).

Cumulatively, these data demonstrate that SNRs and optical clearing are augmented by AT-HP, whereas AT-OC clears tough fibrous tissue whilst also minimizing tissue background noise. Based on these findings, we hypothesized that sequential use of AT-HP followed by AT-OC, termed Atacama Clear (ATC, Fig. 2C-E), would facilitate efficacious tissue optical clearing and 3D imaging of challenging tissue types. To begin to test this, the capacity of ATC to optically clear whole murine organs was tested, with a focus on muscle systems that represent the greatest challenge. ATC cleared intact muscular organs including the heart, UUT, bladder, intestine, and stomach, as well soft tissue organs, such as the lungs (Fig. 2F). Measurement of kidney or heart tissue before and after treatment also demonstrated that ATC does not cause expansion or shrinkage of samples (Supplemental Fig. 2H, I).

Multiplex 3D imaging with ATC

The accurate preservation of tissue morphology, efficacious optical clearing, and high SNRs provided by ATC suggested that this methodology could be used to overcome challenging imaging studies. To test this, we chose to image renal nephrons, the most autofluorescent segment of the kidney and among the highest of any tissue. Indeed, the native global architecture of different nephron segments remains to be directly imaged. Thus, we used ATC to image parvalbumin and ENAC that mark adjacent distal convoluted and connecting tubule nephron segments, respectively [12,13]. As shown in Fig. 3 and Supplemental Movie 2, these tissue regions were distinctly visualized. Critically, we were able to interrogate the 3D structure of these tissues, such as connecting tubule length (Fig. 3B), with single cell resolution (Fig. 3C). Thus, ATC facilitated 3D imaging of previously undocumented tissues, with cellular resolution.

We next examined the heart to determine the efficacy of ATC to image muscular organs. Murine hearts were stained for the arterial vasculature and imaged using ATC (SMA, red, Fig. 4A, B). Despite using low light conditions and diffuse illumination of low magnification stereo fluorescent microscopy, the cardiac arterial bed was nonetheless readily visualized (Fig. 4A, inset). Confocal microscopy was next used to determine the capability of imaging deep inside the organ. Imaging was done through the dense ventricular myocardium. Analyses of the individual slices constituting the 3D image of the heart showed no loss of labeled vessel signal intensity as deep as 1.6 mm into the heart, which was the microscopic focal working distance limit (Fig. 4A, B, and Supplemental Fig. 3).

Studies were next performed to 3D image distinct tissue compartments of the heart. Specifically, we aimed to visualize the sinoatrial node (SAN), the pacemaker of the heart [11]. It is well established that the SAN specifically exhibits robust expression of the HCN4 pacemaker ion channel [23,24]. However, 3D imaging of the SAN have only shown diffuse levels of HCN expression. To this end, ATC was used to image whole hearts immunolabeled with HCN4 to mark the SAN, and Troponin-T to mark the working myocardium. Strikingly, HCN4 distinctly marked the SAN along the terminal crest of the right atria, the known anatomical site of the cardiac pacemaker (Fig. 4C-E). Independent validation by staining solely with DAPI and HCN4 confirmed that

HCN4 is indeed highly expressed and restricted to the terminal crest of the right atria. Thus, we demonstrate that ATC facilitates high resolution imaging of specialized conduction system elements of the heart.

A key determinant of usability for an optical clearing protocol is its capacity to preserve fluorescent *in vivo* labels and endogenous fluorescent reporter proteins. Thus, we tested the preservation of fluorescent signals when using ATC. Intravital dye labeling of blood conducting vessels was performed in neonatal murine pups [25,26], when complex vascular remodeling is occurring, notably in the eye. Half-mounted heads were isolated, optically cleared with ATC, and imaged by confocal microscopy. Results showed a robust preservation of fluorescently labeled cranial and facial vessels throughout the head (Fig. 5A), and high magnification analyses provided a detailed 3D view of the intricate vascular bed perfusing the neonatal eye cup and retina (Fig. 5B and Supplemental Movie 3). ATC provided a sophisticated modality to characterize an organ's cellular structures when combined with intravital dye labeling plus IF. This is shown in Figure 5C, D, where the vasculature of exposed neonatal torsos was immunolabeled post intravital dye labeling. The endogenous intravital dye labeling (red) was readily distinguishable from the immunolabeled vasculature (green, Endomucin), and at high magnification enabled the visualization of mature vessels that conduct blood (yellow) versus immature vessels (green only) that are not yet perfused (Fig. 5D, and Supplemental Movie 4).

The compatibility of ATC with endogenous fluorescent reporter proteins was examined in several experimental model systems. Embryoid bodies (EBs) derived from murine stem cells with a doxycycline-inducible GFP were treated with and without doxycycline, immunostained for E-cadherin (red) to label all cells, and cleared with ATC. GFP was readily detected in the doxycycline-induced EBs (Fig. 6A), but was lacking in control EBs without induction (Fig. 6A, inset). GFP was also readily imaged in the ventricles of adult zebrafish hearts expressing GFP from a cardiomyocyte-specific transgenic promoter (Fig. 6B-D). Treatment with ATC mitigated the autofluorescence in the zebrafish trunk, while preserving the GFP expression in the heart (Fig. 6B, before, Fig. 6C, after ATC). Critically, GFP expression was detected in the ventricular myocardium, but not in the non-contracting bulbus arteriousus of these hearts (Fig. 6D, inset, DAPI). Finally, we used ATC to image kidneys from adult *Spry4*$^{H2B\text{-}Venus}$ transgenic mice expressing Venus fluorescent protein in renal interstitial cells [27]. As shown in Fig. 6E, Venus signal was efficiently preserved as demonstrated by brightly labeled Venus+

interstitial cells (arrows) surrounding the renal tubules of the kidney, overcoming the high background typically associated with renal tissue. To further establish usability, we performed immunolabeling of *Spry4*$^{H2B\text{-}Venus}$ renal tissue. Interestingly, we found that the renal artery contains a previously undocumented population of Venus+ interstitial cells (Fig. 6F, G), which are known to play an important role in controlling vascular tone and compliance [26]. Taken together, these data demonstrate that ATC can be used in complex imaging studies, including those with endogenous fluorescent labels and reporter proteins, with minimal background noise and autofluorescence that facilitates high signal-to-noise ratios, in a broad range of experimental model systems.

Finally, we used ATC to interrogate human kidney biopsies. Due to its more robust proteinaceous extracellular and cellular consistency, human tissue is well known known to be tougher and more autofluorescent than counterpart tissue from smaller mammalian animal models that are commonly used for research, such as mice [1]. To this end, we aimed to determine if the different tissue layers of the glomerulus could be visualized in human samples, as was possible with murine renal tissue. Human samples were stained for Podocalycin, PDGFR-β, and CD31 to mark the podocyte, mesangium and endothelial layers of the glomerulus, respectively. Strikingly, all three tissue layers were distinctly imaged, with single cell resolution (Figure 7). Thus, ATC serves to 3D image both animal and human tissue samples with high resolution.

Discussion

We developed ATC, an aqueous optical clearing protocol designed specifically to address challenges associated with 3D imaging tough fibrous tissues that are resistant to optical clearing, and those that naturally exhibit high autofluorescence. This protocol is useful for interrogating tissues such as the kidney, which exhibits high autofluorescence, and the heart that exhibits robust autofluorescence and is resistant to optical clearing. ATC is a two-stage method, with an initial tissue treatment step with AT-HP that removes blood, serves to decrease tissue autofluorescence, and increases tissue optical clearing. AT-HP was established to significantly decrease tissue autofluorescence in a time-dependent manner. This serves as a useful property of AT-HP, as investigators can vary the time of use to fit the autofluorescence of specific samples. Strikingly, we discovered that AT-HP potentiated the tissue clearing capacity of all the published optical clearing reagents

tested. This adds to the benefits of AT-HP, as it can potentially be integrated into already established working protocols to mitigate autofluorescence and enhance tissue transparency.

After treatment with AT-HP, tissue is optically cleared with AT-OC, a refractive index matching solution comprised of formamide and glycerol. Formamide was chosen for optical clearing as we discovered it produced a moderate, statistically significant reduction in autofluorescence. By contrast, similar benefits were not observed with reagents such as quadrol or MXDA that are currently used in optical clearing methods. Notably, we demonstrate that the combination of glycerol with formamide provides greater tissue clearing than protocols such as ClearT^2 that also use formamide. Indeed, we demonstrate that the sequential use of AT-HP and then AT-OC, constituting the two-stage ATC protocol, provides robust optical clearing. With a focus on muscle, among the most difficult tissue type to clear, we demonstrate that ATC can render transparent whole murine muscular organs, including the heart, stomach, upper urinary system, intestine, and bladder.

The mitigation of tissue background noise, as is seen with AT-HP and AT-OC, is only beneficial if it is consistent with an increase in SNRs. To this end, we compared ATC imaging to CUBIC, a leading aqueous optical clearing methodology. Using adjacent tissue sections of the same heart and kidney, imaged in the same field of view, we demonstrate that tissue imaged with ATC exhibits approximately 50% less background noise, and consequently, labeled structures exhibited over two-fold higher SNRs. Moreover, we demonstrate that the enhanced SNRs provided by ATC facilitates challenging imaging studies of intricate structures of the heart and kidney. For instance, we used ATC to image the previously undocumented gross architecture of connecting and distal convoluted tubule segments of nephrons, which exhibit among the highest known tissue autofluorescence. Additionally, we were able to distinctly visualize the SAN pacemaker of the heart in 3D by its specific, robust expression of HCN4 along the terminal crest of the right atria.

ATC was shown to be compatible with fluorescent tracers and reporter proteins, which is critical for the usability of an optical clearing technology. Using intravital dye labeling, we were able to visualize the complex 3D architecture of the ocular vasculature, as well as nascent and patent vessels of the murine trunk. Moreover, ATC was compatible with visualization of GFP-expressing stem cell-derived EBs, GFP-expressing zebrafish

hearts, murine kidneys expressing Venus fluorescent proteins in renal interstitial cells. Thus, ATC can be used for imaging across different transgenic animal and 3D stem cell model systems. We sought to develop ATC for multiplex imaging studies of challenging tissue types, including of human specimens. Indeed, human tissues can be tougher and exhibit higher autofluorescence than that of small research animals like mice. To this end, we validated that ATC facilitates imaging of human kidney biopsies that exhibit robust autofluorescence. The unique architecture of the renal glomerulus was interrogated by multiplex immunofluorescence, and we readily visualized the endothelial, podocyte, and mesangial glomerular tissue layers with cellular resolution. Thus, ATC can serve as a valuable tool to image human clinical samples.

In summary, we developed an optical clearing technology, ATC, to perform 3D imaging that is challenged by the high background noise of samples, or their resistance to optical clearing. ATC was validated for use in cell and animal model systems of different species, including those expressing endogenous fluorescent reporter proteins. The enhanced SNRs and optical clearing properties will make it a powerful imaging tool for basic science research studies, as well as studies of human clinical samples.

METHODS

Animals

Adult mice were purchased from Taconic Farms (Germantown, NY, USA). Spry4$^{H2B\text{-}Venus}$ mice expressing Venus fluorescent reporter protein from the endogenous Spry4 locus has been previously described [27]. The transgenic zebrafish Tg(*myl7:EGFP*) reporter line has been described [28]. All animals were housed at an AAALAC accredited facility at the Weill Medical College of Cornell University Animal Facility. All experiments were approved and carried out in accordance with the ethical guidelines and regulations stipulated by the Institutional Animal Care and Use Committee of Weill Medical College of Cornell University.

Atacama Clear

Organs were immersion fixed with 4% paraformaldehyde (PFA) at 4°C using a rotisserie-style shaker. Fixation time was modulated according to tissue thickness, and whether organs were of soft tissue or muscular tissue type. Sufficient time of fixing was required for adequate preservation of antigens. Three week-old whole adult

mouse hearts and kidneys were fixed for 72 hrs, mouse neonatal tissues and adult zebrafish hearts were fixed for 24 hrs, and stem cell-derived EBs were fixed for 3 hrs. After fixation, it was critical to quench free fixative to obtain reproducible immunostaining results. To this end, fixed tissues were rinsed with copious amounts of PBS, and free fixative quenched by immersing organs in .5M Tris, pH 7.5, at 37 ^{O}C typically for 12 hours (overnight incubation), and at minimum for 1 hour [29,30]. Tissues were then rinsed with copious amounts of PBS, and stored at 4 ^{O}C until use. Note, all steps of fixing and ATC protocol are done using rotisserie-style shaker to ensure proper penetration of solutions.

ATC consists of two stages: stage 1 is treatment with AT-HP, followed by stage 2, or treatment with AT-OC. The base solution of AT-HP consists of the following final concentrations: 10mM EDTA, 150mM KCl, 0.5% Triton-X (v/v), 20% DMSO (v/v), 0.5% NaN3 (w/v), 100 mM Tris, pH 9.5 made in basic double distilled H_20 (pH 9 with NaOH; final pH of base solution is 9.5). Base solution is mixed well, and then allowed to settle for 10 minutes. Right before use, H_20_2 is directly added to AT-HP base solution. To start, a final concentration of 0.05% H_20_2 is always used (diluted from 30% stock solution v/v, Sigma, H1009). AT-HP containing 0.05% H_20_2 is mixed well, and the allowed to acclimate at RT for 10 minutes. Organs are then submerged in AT-HP within a suitable receptacle, such as an Eppendorf tube or cryogenic vial, and gently rocked on a rotisserie shaker at room temperature. Tissues are observed to ensure that air pockets are not accumulating within the tissue; minor bubbling at the edges of tissues is permissible. In instances where robust oxygenation was observed, the reaction was stopped by rinsing tissue in PBS, and the reaction mixture was adjusted to proceed more slowly by lowering the concentration of H_20_2 to 0.01%. Once oxygenation was confirmed to be lacking, samples were incubated in AT-HP at room temperature for 2 hours in the dark. AT-HP was then removed, tissues rinsed with water 2x, and then washed with PBS for 5 min at room temperature. Tissue was then incubated with wash buffer comprised of 10mM EDTA, 150 mM KCl, 10% DMSO, and 20 mM Tris, pH 9.5 dissolved in basic DDH_20 for 20 min at 37 ^{O}C. Tissue decolorization and autofluorescence was then assessed. If further processing is needed, a new round of fresh AT-HP treatment was done by increasing the concentration of H_20_2 by 0.05%. In this manner, AT-HP treatment can continue until desired results by increasing the concentration of H_20_2. The maximum concentration of H_20_2 required for our studies was 1%.

After AT-HP treatment, samples were amenable to previously established standard immuno-staining protocols. For our studies, tissues were rinsed 3 x 5 min with PBS + 0.5% triton-x (PBST), and then permeabilized in blocking solution consisting of PBST + 1% NDS + 1% DMSO overnight at 37 ^{O}C. Primary antibodies were then incubated in PBST + 1% DMSO. Antibodies used in this study were: anti-α-smooth muscle actin (clone 1A4, Sigma, at 1:2000), anti-ENAC (Ergonul et al., at 1:200) [31], anti-parvalbumin (R&D AF5058, at 1:200), anti-endomucin (ab106100, Abcam, at 1:200), anti-podocalyxin (3169, R&D Systems, at 1:200), anti-HCN4 (APC-052, Alomone, at 1:500), anti-Pdgfr-β (3169, Cell Signaling Technology, at 1:100), anti-CD31 (BD Biosciences, 550389 at 1/500), anti-E-cadeherin (610181, BD Biosciences, at 1:200), and cardiac Troponin-T (NB110-2546, R&D Systems, at 1:500). Minimally cross-absorbed Alexa Flour secondary antibodies were used to detect primary antibodies.

Optical clearing with AT-OC was next performed to render immunostained tissue transparent. Optical clearing with AT-OC consisted of impregnating samples with sequential solutions of varying formamide/glycerol concentrations, with each solution rendering tissue increasingly more transparent (deionized formamide, Sigma, F7503; ultrapure glycerol, ThermoFisher, AC410985000). Specifically, tissues were immersed with the following the following sequence of solutions made in basic DDH_20 at 37 ^{O}C: 20% formamide + 0.5% Triton-x, 20% formamide x 3, 20% formamide/5% glycerol, 20% formamide/10% glycerol, 20% formamide/25% glycerol, 20% formamide/ 50% glycerol, 30% formamide/70% glycerol, and then a final solution comprised of 17% formamide + 5% Triethalomine + 70% glycerol + 3% Tris (w/v, Tris, Promega, H5135) made in basic DDH_20. At the onset, tissues are incubated with 20% Formamide + .5% Triton-x overnight to prime the tissue for optical clearing. Traces of Triton-x are then removed by washing with 20% Formamide 3x. The time of incubation in each solution varied depending on the tissue being cleared, in particular due to the fact that the viscosity of clearing solutions increases with rises in glycerol concentration. Thus, care is needed to ensure that the entire tissue has been impregnated with the current solution before moving forward to subsequent solutions. Penetration of clearing mixtures into samples could be ascertained by ensuring samples sank to the bottom of containers. For large organs, dabbing tissue clear of solutions before adding the subsequent mixture further facilitated optical clearing. As a guideline, the number of solutions could be reduced to enable faster clearing if working with thinner or sectioned tissue. In such instances, treatment could start with 20% formamide +.5%

triton-x, then 20% formamide alone, followed by quarter percent increases of glycerol, starting with 20% formamide/25% glycerol. Moreover, the entire sequence of solutions was not needed to optically clear all tissue, e.g. 0.5 mm kidney sections were rendered transparent with 20% formamide/25% glycerol. After clearing, tissue were imaged directly in final clearing solution, using glass bottom plates with spacers, and then placing a coverslip over the sample to ensure it does not move. Samples could be stored in final clearing solution for months. Confocal microscopy was done on a Zeiss LSM 800 and stereo fluorescence microscopy on a Nikon SMZ1500 mounted with a Nikon DS-FI3 camera. 3D analyses were performed using Imaris Imaging Software (Bitplane).

Intravital Dye Labeling

Intravital dye labeling was performed as previously described [25]. In short, 100 µl of fluorescently tagged tomato lectin (0.2mg/ml in PBS, Vector laboratories) was injected into the circulation of anesthetized newborn pups (postnatal day zero) by intracardiac injection. Pups were euthanized after a 5 min period to let the lectin circulate, and tissues harvested and fixed.

Stem cell-derived embryoid bodies

Mouse embryonic stem cells (mESCs) with a doxycycline inducible GFP transgene [32] were maintained on gelatin coated tissue culture treated plates in serum-free conditions. Media (2i plus LIF) was composed of 50% Neurobasal media (Gibco) and 50% DMEM/F12 (Corning cellgro) supplemented with 0.5X N2 and 0.5X B27 (Gibco), 100U/mL Penicillin, 0.1 mg/ml Streptomycin (Corning), 0.05% BSA (Gibco), 2mM Glutamine (Corning), 0.15 mM monothioglycerol (Sigma), 1000U/ml mouse LIF (ESGRO, Sigma), 3uM CHIR99021 (Stem Cell Technologies), and 1uM PD0325901 (Stem Cell Technologies). To produce embryoid bodies (EBs) mESCs were differentiated in serum free differentiation media (SFD). SFD consisted of 75% IMDM (Gibco), 25% Ham's F12 (Corning cellgro), 0.5X N2 (Gibco), 0.5X B27 (Gibco), 0.05% BSA (Gibco), 0.5mM Ascorbic Acid (Sigma), 2mM Glutamine (Corning), 0.45 mM monothioglycerol (Sigma), 100U/mL Penicillin and 0.1 mg/ml Streptomycin (Corning). On the first day of differentiation, mESCs were dissociated with Accutase (Sigma) and plated at 40,000 cells/ml in 12.5ml of SFD in 100mm petri dishes. After 48 hours, EBs were dissociated with Accutase and plated again at 80,000 cells/ml in SFD supplemented with 75ng/ml Activin A

(R&D Systems). After 24 hours, expression of GFP was induced by adding Doxycycline (Sigma) for 24 hours before EBs collection.

ACKNOWLEDGEMENTS

This work was supported by an NIH NIDDK R21 DK116171 grant and Mastercard Diversity-Mentorship Collaborative Pilot Grant to R.H. Support to N.D.S. was by the Weill Cornell Hartman Foundation for Therapeutic Organ Regeneration. We thank Dr. Miriam Gordillo for providing EB samples. We thank Dr. Lawrence Palmer for providing advice on nephron staining and ENAC antibody.

AUTHOR CONTRIBUTIONS

Study conception, R.H.; Technological Conception and Development, R.H.; Experiment Design, R.H., T.E., E.A.J; Experiments, R.H., N.D.S., L.L.; Intellectual Contributions, R.H., T.E., E.A.J.; Manuscript Writing, R.H. with input from T.E., E.A.J.

DECLARATION OF INTERESTS

R.H. is inventor on a U.S. patent relating to optical clearing technology submitted by the Center for Technology Licensing at Cornell University.

FIGURE LEGENDS

Figure 1. Enhanced signal-to-noise ratios using AT-HP. A) Green autofluorescence of different murine organs imaged in the same field of view by stereo fluorescent microscopy, including the kidney, heart, and spleen. **B)** Green autofluorescence of a single kidney cut in two, with one half left untreated and the other half treated with AT-HP. **C)** Red autofluorescence of control and AT-HP treated kidney. **D)** Quantification of decrease in green and red autofluorescence with AT-HP treatment. **E-J)** A single kidney (E-G) and heart (H-J) were cut into 500 µm sections, and adjacent sections treated with CUBIC1 (CU1) or AT-HP. Bright field images of adjacent sections side-by-side in the same field of view were taken for comparison of decolorization and tissue morphology (E, F, H, I). Green autofluorescence of tissue sections treated with CU1 or AT-HP were imaged side by side in the same field of view (G, J). **K)** Quantification of levels of green autofluorescence in adjacent tissue sections treated with CU1 or AT-HP. $p<0.0001$ **L-Q)** Adjacent 500 µm sections of a single kidney (L-N) and heart (O-Q) were treated with CU1 or AT-HP, and IF performed for the renal and cardiac arterial bed (SMA, green). Low magnification fluorescence images of adjacent sections imaged side-by-side were taken to provide direct comparison of CUBIC and Atacama based IF (L, O). Analyses of arterial staining was further assayed at high magnification (M, N, P, Q). **R**) Quantification of IF signal-to-noise ratio in sections treated with CU1 or AT-HP. $p<0.0001$ **S-V)** Triple multiplex IF imaging for the distinct tissue compartments of the murine glomerulus (S, arrow points to region shown at higher magnification), including the podocyte (T, podocalyxin), mesangial (U, PDGFR-β), and endothelial (V, endomucin) tissue layers (see also Supplementary Movie 1).

Figure 2. Optical Clearing with ATC. A) 500 µm sections obtained from a single kidney were left untreated or treated with AT-HP, and then imaged in the same field of view after treatment with published aqueous optical clearing reagents, including quadrol, urea, formamide, glycerol, sorbitol, fructose, sucrose and DMSO. **B)** Quantification of optical clearing capacity with AT-HP. **C-E)** Representative workflow of ATC optical clearing, showing an unperfused 500 µm heart section (C) being first treated with AT-HP (D) and subsequently with AT-OC. This two-stage protocol was termed ATC. **F**) Representative ATC optical clearing of whole murine

muscular organs, including heart, upper urinary tract (UUT), bladder, intestine, and stomach; and soft tissue organs, such as the lung.

Figure 3. 3D imaging of distinct nephron segments using ATC. A-C) ATC was used to 3D image nephron segments that are known to exhibit notoriously high autofluorescence. Kidney sections were stained for ENAC (red) and Parvalbumin (green) to mark adjacent connecting and distal convoluted tubule nephron compartments, respectively. ATC readily facilitated the distinct visualization of each nephron segment, as well as their gross architectural tissue arrangement (A; also see Supplemental Movie 2). **B)** The high SNRs obtained using ATC facilitated direct measurements of tubule dimensions (B, demarked measurement of connecting tubule length in 3D = 188 µm), and provided single cell resolution (C).

Figure 4. 3D imaging of specialized cardiac tissue compartments using ATC. A-B) ATC was used to visualize the arterial bed of the heart (VSMA, red). Both low magnification stereomicroscopy (A, inset) and confocal microscopy (A, B) readily facilitated imaging of cardiac arteries. Confocal imaging showed ATC facilitated imaging 1.6 mm deep inside the heart without loss of signal intensity (B, x-axis view; also see Supplementary Fig. 3, showing all the representative slices of the 3D image). **C-E)** ATC was used to visualize the specialized pacemaker cells of the cardiac conduction system. Hearts were first stained for the working myocardium (cTroponin-T, green) and sinoatrial pacemaker node (HCN4 pacemaker channels, red). 3D interrogation showed that the SAN localized to the terminal crest (TC) of the right atrium (4C; inset shows SAN alone). Independent validation by staining solely with DAPI and HCN4 confirmed that HCN4 pacemaker channels are highly expressed and restricted to the anatomical site of the SAN, the terminal crest of the right atria (4D, merged; 4E, HCN4). RA, right atrium; LA, left atrium; TC, terminal crest

Figure 5. ATC is compatible with *in vivo* tracers. A, B) 3D imaging of half mounted neonatal murine heads cleared with ATC after intravital dye labeling (IVDL, tomato lectin) of the circulatory system validated compatibility with *in vivo* tracers (A, facial vasculature; B, high magnification of the eye vasculature; also see Supplemental Movie 3). **C, D)** Confocal imaging of neonatal body trunks cleared with ATC after intravital dye labeling of blood conducting vessels (red) and IF for the whole vasculature (vascular endothelium, endomucin,

green). High magnification analyses (D) enabled visualization of patent blood conducting vessels (yellow) and nascent unperfused vessels (green; also see Supplemental Movie 4).

Figure 6. ATC is compatible with fluorescent reporter proteins. A) 3D imaging of intact ATC cleared stem cell-derived EBs exhibiting doxycycline-inducible GFP expression and immunolabeled for E-cadherin (Inset, control organoids lacking doxycycline treatment). **B-D)** Imaging of whole zebrafish exhibiting GFP expression in the ventricular myocardium of the heart showed a decrease in autofluorescence (AF) and retained GFP expression (B, before ATC treatment; C, after ATC treatment). 3D imaging through intact hearts validated GFP expression localized to the ventricular myocardium (D; Inset, DAPI). **E)** ATC cleared adult murine *Spry4*$^{H2B\text{-}Venus}$ kidneys exhibiting Venus fluorescent reporter protein expression in renal interstitial cells (arrows mark interstitial cells). **F, G)** Low and high magnification 3D imaging of ATC cleared *Spry4*$^{H2B\text{-}Venus}$ kidneys immunolabeled for smooth muscle actin (SMA, red) revealed a Venus+ interstitial cell population localized to the renal artery (G, Venus+ interstitial cells, arrows).

Figure 7. ATC readily facilitates multiplex IF imaging of human renal tissue. A-E) ATC was used to perform 3D multiplex imaging of distinct glomerular tissues (A, low magnification image; arrow points to region shown at high magnification). Samples were immunostained for endothelial (B, CD31, red), mesangial (C, PDGFR-β, blue) and podocyte (D, podocalyxin, green) tissue compartments (E, all merged). All tissue regions could be distinctly visualized, with cellular resolution (inset shows high magnification of region demarked by white brackets in panels B-E).

Supplemental Figure 1. Development of AT-HP. A, B) Bright field image (A) and green autofluorescence (B) of kidneys that perfused with different efficiencies. Kidney with more robust blood content exhibited higher autofluorescence. **C, D)** Bright field image (C) and green autofluorescence (D) of perfused hearts showed that regions of the organ that retained robust amounts of blood, such as the ventricle (arrow head), exhibited higher autofluorescence than regions that were readily cleared of blood, such as the left and right atria (arrow). **E, F)** Optically cleared half mounted hearts showed that regions that were devoid of blood readily became transparent (region 1), whereas regions flush with blood (region 2) were resistant to clearing (F, quantification

of transparency in regions devoid of blood, or region 1 vs. region with robust amounts of blood, or region 2. $p<0.0001$). **G, H)** Bright field images of heart (G) and kidney (H) tissue morphology after treatment with standard H_2O_2 (arrow heads point to sites of tissue tearing; arrows point to oxygen pockets trapped within tissue). **I, J)** Autofluorescence of tissue before (I) and after (J) standard H_2O_2 treatment. Arrows point to regions of tissue damage after H_2O_2 treatment that then exhibited increased autofluorescence. **K)** Screen for inhibitors of H_2O_2 generated tissue oxygenation; heart sections treated with H_2O_2 plus sodium azide (NaN3), EDTA, L-ascorbic acid (L-Asc), L-cysteine (L-Cys), cadmium (Cd^{2+}), zinc (Zn^{2+}), and magnesium (Mg^{2+}), and. **L-N**) Images of a whole kidney before (L) and after (M) treatment with AT-HP. (N) Bright field image of representative kidney section morphology after treatment. **O-Q)** Images of a 1 mm heart section before (O) and after (P) treatment with AT-HP. (Q) Bright field image of representative heart section morphology after treatment. **R-T)** Time dependent decrease in autofluorescence of halved kidney treated with AT-HP. **U-W)** Time dependent decrease in autofluorescence of 1 mm heart section treated with AT-HP.

Supplemental Figure 2. Development of AT-OC. A-D) Green autofluorescence of tissue before and after treatment with reagents from $ClearT^2$ (A, formamide), MACS (B, m-Xylylenediamine, MXDA), and CUBIC (C, quadrol) optical clearing techniques. **D)** Quantification of mean change in tissue autofluorescence after treatment with optical clearing reagents. **E, F)** Optical clearing of heart sections of different thickness with $ClearT^2$ or AT-OC. **F)** Quantification of optical clearing with $ClearT^2$ or AT-OC. **G)** Optical clearing of 1 mm heart section after aortic arch perfusion, and then treatment with AT-OC. **H, I)** Measurements of 1mm thick kidney (H) and heart (I) sections before and after treatment with ATC showed no change in sample size.

Supplementary Figure 3. **Efficacy of imaging deep inside organs with ATC. A)** All representative image slices comprising the 3D image of whole hearts immunolabeled for cardiac arteries and imaged with ATC (see Fig. 4A, B). **B)** Quantification of max IF signal intensity throughout the depth of imaging showed no loss of signal as deep as 1.6 mm.

Supplemental Movie 1. 3D Imaging of the renal glomerular tissue architecture

Supplemental Movie 2. 3D imaging of distal convoluted tubule and connecting duct nephrogenic zones

Supplemental Movie 3. 3D imaging of the perfused murine face and ocular vasculature

Supplemental Movie 4. 3D imaging of the perfused and nascent vasculature in the murine trunk

REFERENCES

1 Richardson, D. S. & Lichtman, J. W. Clarifying Tissue Clearing. *Cell* **162**, 246-257, doi:10.1016/j.cell.2015.06.067 (2015).

2 Yu, T., Zhu, J., Li, D. & Zhu, D. Physical and chemical mechanisms of tissue optical clearing. *iScience* **24**, 102178, doi:10.1016/j.isci.2021.102178 (2021).

3 Hama, H. *et al.* Scale: a chemical approach for fluorescence imaging and reconstruction of transparent mouse brain. *Nat Neurosci* **14**, 1481-1488, doi:10.1038/nn.2928 (2011).

4 Hama, H. *et al.* ScaleS: an optical clearing palette for biological imaging. *Nat Neurosci* **18**, 1518-1529, doi:10.1038/nn.4107 (2015).

5 Kuwajima, T. *et al.* ClearT: a detergent- and solvent-free clearing method for neuronal and non-neuronal tissue. *Development* **140**, 1364-1368, doi:10.1242/dev.091844 (2013).

6 Ke, M. T., Fujimoto, S. & Imai, T. SeeDB: a simple and morphology-preserving optical clearing agent for neuronal circuit reconstruction. *Nat Neurosci* **16**, 1154-1161, doi:10.1038/nn.3447 (2013).

7 Hou, B. *et al.* Scalable and DiI-compatible optical clearance of the mammalian brain. *Front Neuroanat* **9**, 19, doi:10.3389/fnana.2015.00019 (2015).

8 Susaki, E. A. *et al.* Whole-brain imaging with single-cell resolution using chemical cocktails and computational analysis. *Cell* **157**, 726-739, doi:10.1016/j.cell.2014.03.042 (2014).

9 Tainaka, K. *et al.* Whole-body imaging with single-cell resolution by tissue decolorization. *Cell* **159**, 911-924, doi:10.1016/j.cell.2014.10.034 (2014).

10 Matsumoto, K. *et al.* Advanced CUBIC tissue clearing for whole-organ cell profiling. *Nature protocols* **14**, 3506-3537, doi:10.1038/s41596-019-0240-9 (2019).

11 Murphy, C. & Lazzara, R. Current concepts of anatomy and electrophysiology of the sinus node. *Journal of interventional cardiac electrophysiology : an international journal of arrhythmias and pacing* **46**, 9-18, doi:10.1007/s10840-016-0137-2 (2016).

12 Olinger, E., Schwaller, B., Loffing, J., Gailly, P. & Devuyst, O. Parvalbumin: calcium and magnesium buffering in the distal nephron. *Nephrol Dial Transplant* **27**, 3988-3994, doi:10.1093/ndt/gfs457 (2012).

13 Subramanya, A. R. & Ellison, D. H. Distal convoluted tubule. *Clin J Am Soc Nephrol* **9**, 2147-2163, doi:10.2215/CJN.05920613 (2014).

14 Pollak, M. R., Quaggin, S. E., Hoenig, M. P. & Dworkin, L. D. The glomerulus: the sphere of influence. *Clin J Am Soc Nephrol* **9**, 1461-1469, doi:10.2215/CJN.09400913 (2014).

15 Azaripour, A. *et al.* A survey of clearing techniques for 3D imaging of tissues with special reference to connective tissue. *Progress in histochemistry and cytochemistry* **51**, 9-23, doi:10.1016/j.proghi.2016.04.001 (2016).

16 Nagata, M. Glomerulogenesis and the role of endothelium. *Curr Opin Nephrol Hypertens* **27**, 159-164, doi:10.1097/MNH.0000000000000402 (2018).

17 Balbotkina, E. V. & Kutina, A. V. Structure and Properties of the Glomerular Filtration Barrier in Vertebrates: Role of a Charge in Protein Filtration. *Journal of Evolutionary Biochemistry and Physiology* **59**, 1891-1910, doi:10.1134/S0022093023060017 (2023).

18 Chung, K. *et al.* Structural and molecular interrogation of intact biological systems. *Nature* **497**, 332-337, doi:10.1038/nature12107 (2013).

19 Marx, V. Microscopy: seeing through tissue. *Nature methods* **11**, 1209-1214, doi:10.1038/nmeth.3181 (2014).

20 Chen, L. *et al.* UbasM: An effective balanced optical clearing method for intact biomedical imaging. *Scientific reports* **7**, 12218, doi:10.1038/s41598-017-12484-3 (2017).

21 Zhu, X. *et al.* Ultrafast optical clearing method for three-dimensional imaging with cellular resolution. *Proc Natl Acad Sci U S A* **116**, 11480-11489, doi:10.1073/pnas.1819583116 (2019).

22 Zhu, J. *et al.* MACS: Rapid Aqueous Clearing System for 3D Mapping of Intact Organs. *Adv Sci (Weinh)* **7**, 1903185, doi:10.1002/advs.201903185 (2020).

23 Sartiani, L., Mannaioni, G., Masi, A., Novella Romanelli, M. & Cerbai, E. The Hyperpolarization-Activated Cyclic Nucleotide-Gated Channels: from Biophysics to Pharmacology of a Unique Family of Ion Channels. *Pharmacol Rev* **69**, 354-395, doi:10.1124/pr.117.014035 (2017).

24 Ludwig, A. *et al.* Two pacemaker channels from human heart with profoundly different activation kinetics. *The EMBO journal* **18**, 2323-2329 (1999).

25 Hurtado, R. *et al.* Pbx1-dependent control of VMC differentiation kinetics underlies gross renal vascular patterning. *Development* **142**, 2653-2664, doi:10.1242/dev.124776 (2015).

26 Herzlinger, D. & Hurtado, R. Patterning the renal vascular bed. *Seminars in cell & developmental biology* **36**, 50-56, doi:10.1016/j.semcdb.2014.08.002 (2014).

27 Morgani, S. M. *et al.* A Sprouty4 reporter to monitor FGF/ERK signaling activity in ESCs and mice. *Dev Biol* **441**, 104-126, doi:10.1016/j.ydbio.2018.06.017 (2018).

28 Huang, C. J., Tu, C. T., Hsiao, C. D., Hsieh, F. J. & Tsai, H. J. Germ-line transmission of a myocardium-specific GFP transgene reveals critical regulatory elements in the cardiac myosin light chain 2 promoter of zebrafish. *Dev Dyn* **228**, 30-40, doi:10.1002/dvdy.10356 (2003).

29 Sutherland, B. W., Toews, J. & Kast, J. Utility of formaldehyde cross-linking and mass spectrometry in the study of protein-protein interactions. *J Mass Spectrom* **43**, 699-715, doi:10.1002/jms.1415 (2008).

30 de Jonge, W. J., Brok, M., Kemmeren, P. & Holstege, F. C. P. An Optimized Chromatin Immunoprecipitation Protocol for Quantification of Protein-DNA Interactions. *STAR Protoc* **1**, 100020, doi:10.1016/j.xpro.2020.100020 (2020).

31 Ergonul, Z., Frindt, G. & Palmer, L. G. Regulation of maturation and processing of ENaC subunits in the rat kidney. *Am J Physiol Renal Physiol* **291**, F683-693, doi:10.1152/ajprenal.00422.2005 (2006).

32 Holtzinger, A., Rosenfeld, G. E. & Evans, T. Gata4 directs development of cardiac-inducing endoderm from ES cells. *Dev Biol* **337**, 63-73, doi:10.1016/j.ydbio.2009.10.003 (2010).

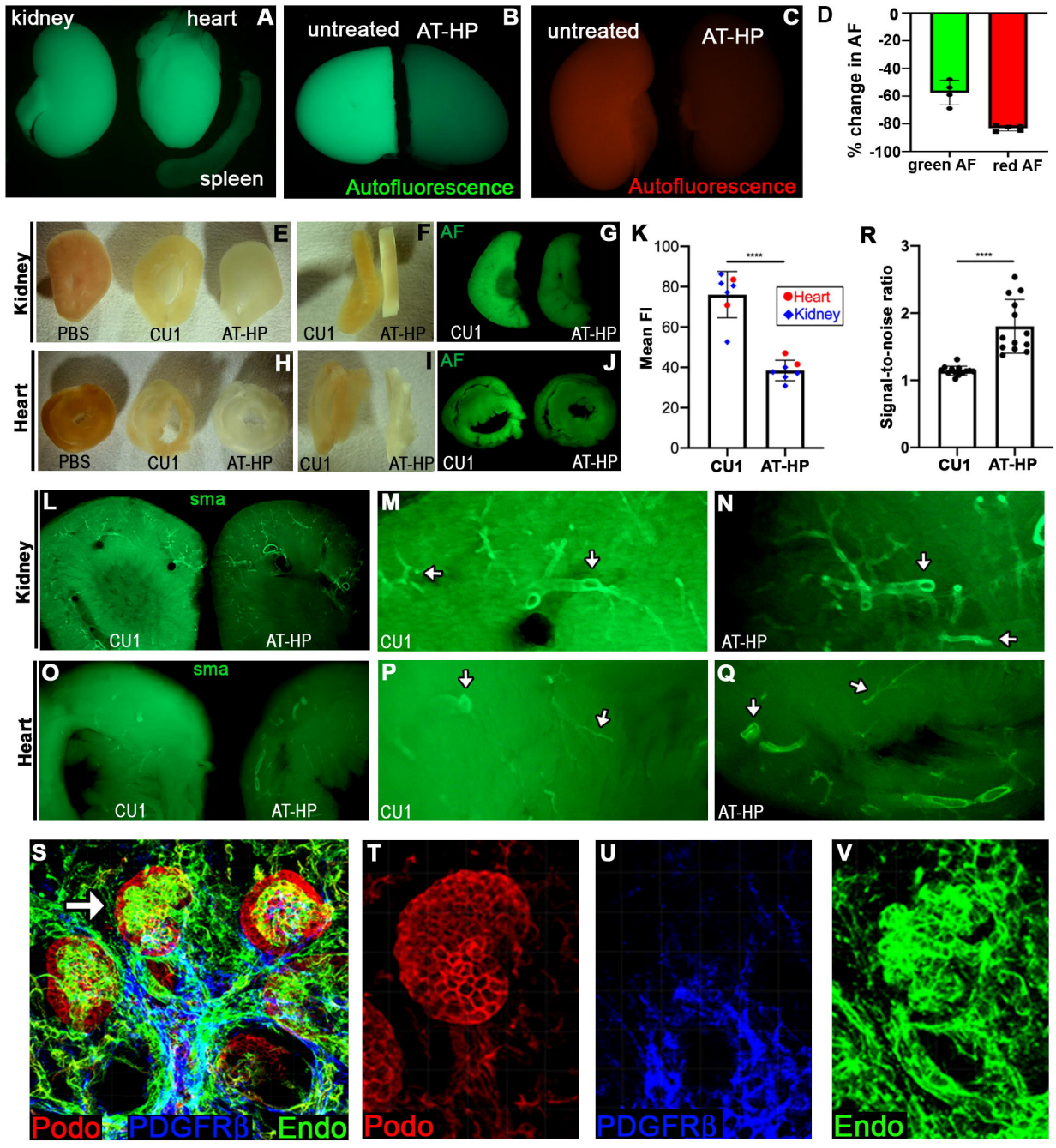
A
kidney
heart
spleen
B
untreated
AT-HP
Autofluorescence
C
untreated
AT-HP
Autofluorescence
D
% change in AF
0
-20
-40
-60
-80
-100
green AF
red AF
Kidney
Heart
E
PBS
CU1
AT-HP
F
CU1
AT-HP
G
AF
CU1
AT-HP
H
PBS
CU1
AT-HP
I
CU1
AT-HP
J
AF
CU1
AT-HP
K
Mean FI
100
80
60
40
20
0
****
Heart
Kidney
CU1
AT-HP
R
Signal-to-noise ratio
3
2
1
0
****
CU1
AT-HP
L
sma
CU1
AT-HP
M
CU1
N
AT-HP
O
sma
CU1
AT-HP
P
CU1
Q
AT-HP
S
Podo
PDGFRβ
Endo
T
Podo
U
PDGFRβ
V
Endo

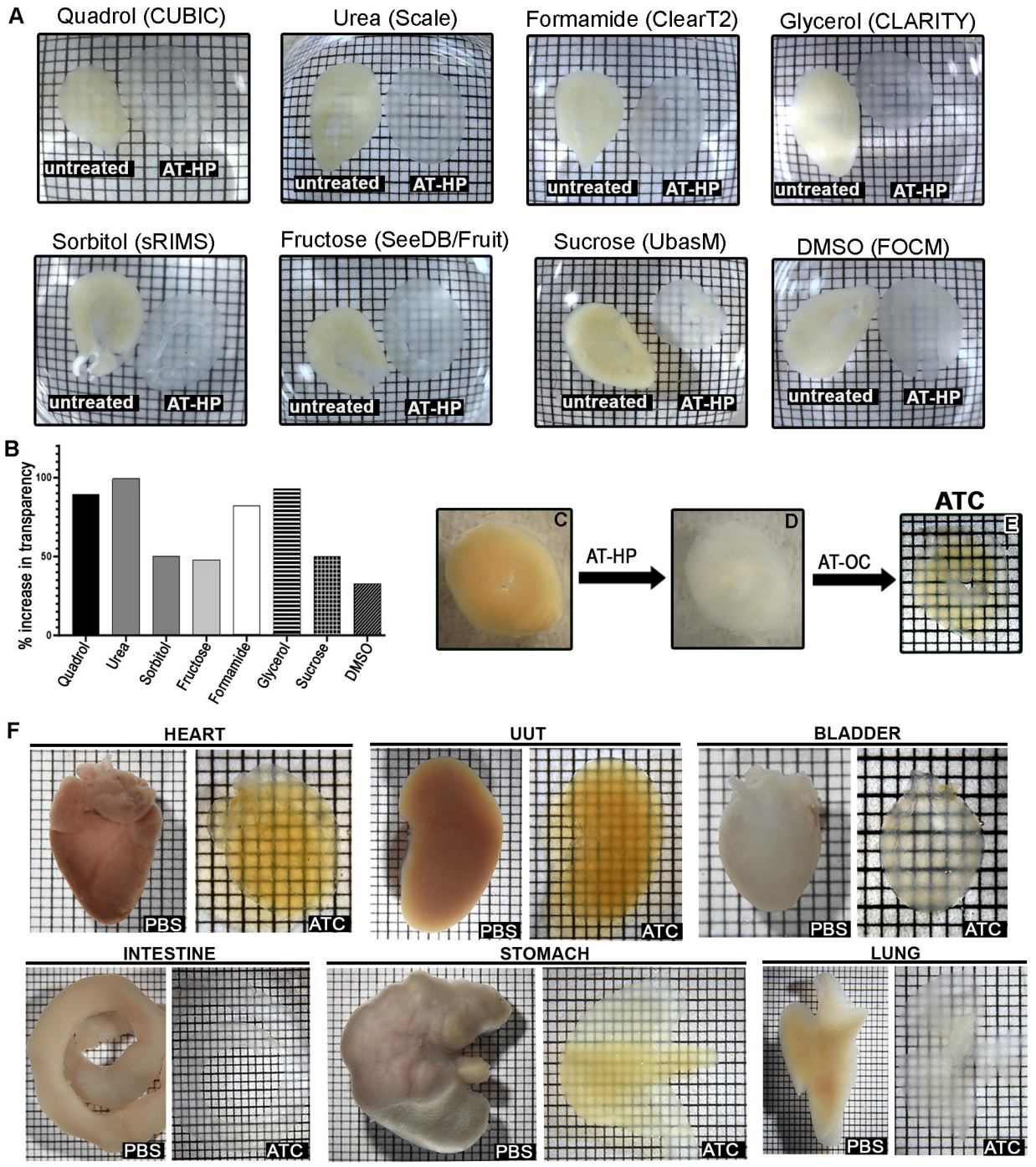
A
Quadrol (CUBIC)
Urea (Scale)
Formamide (ClearT2)
Glycerol (CLARITY)
Sorbitol (sRIMS)
Fructose (SeeDB/Fruit)
Sucrose (UbasM)
DMSO (FOCM)
untreated
AT-HP
B
% increase in transparency
100
50
0
Quadrol
Urea
Sorbitol
Fructose
Formamide
Glycerol
Sucrose
DMSO
C
AT-HP
D
AT-OC
ATC
E
F
HEART
UUT
BLADDER
INTESTINE
STOMACH
LUNG
PBS
ATC

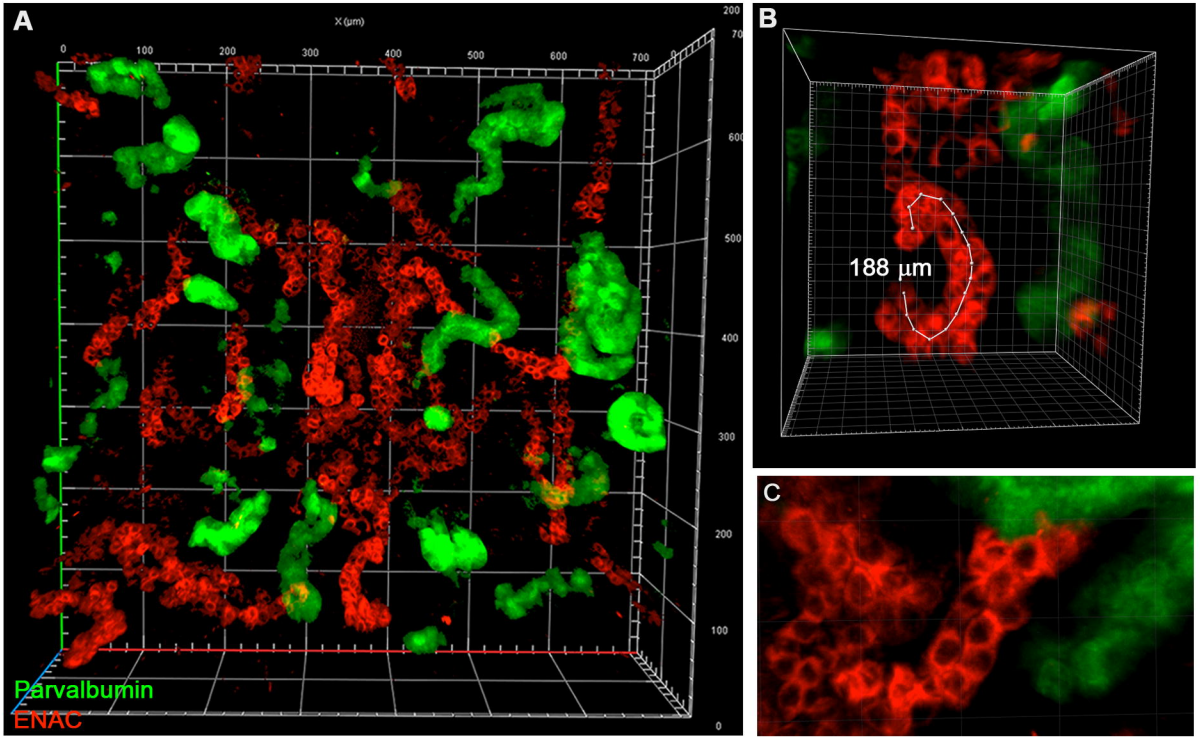
A
X (µm)
0
100
200
300
400
500
600
700
Parvalbumin
ENAC
B
188 µm
C

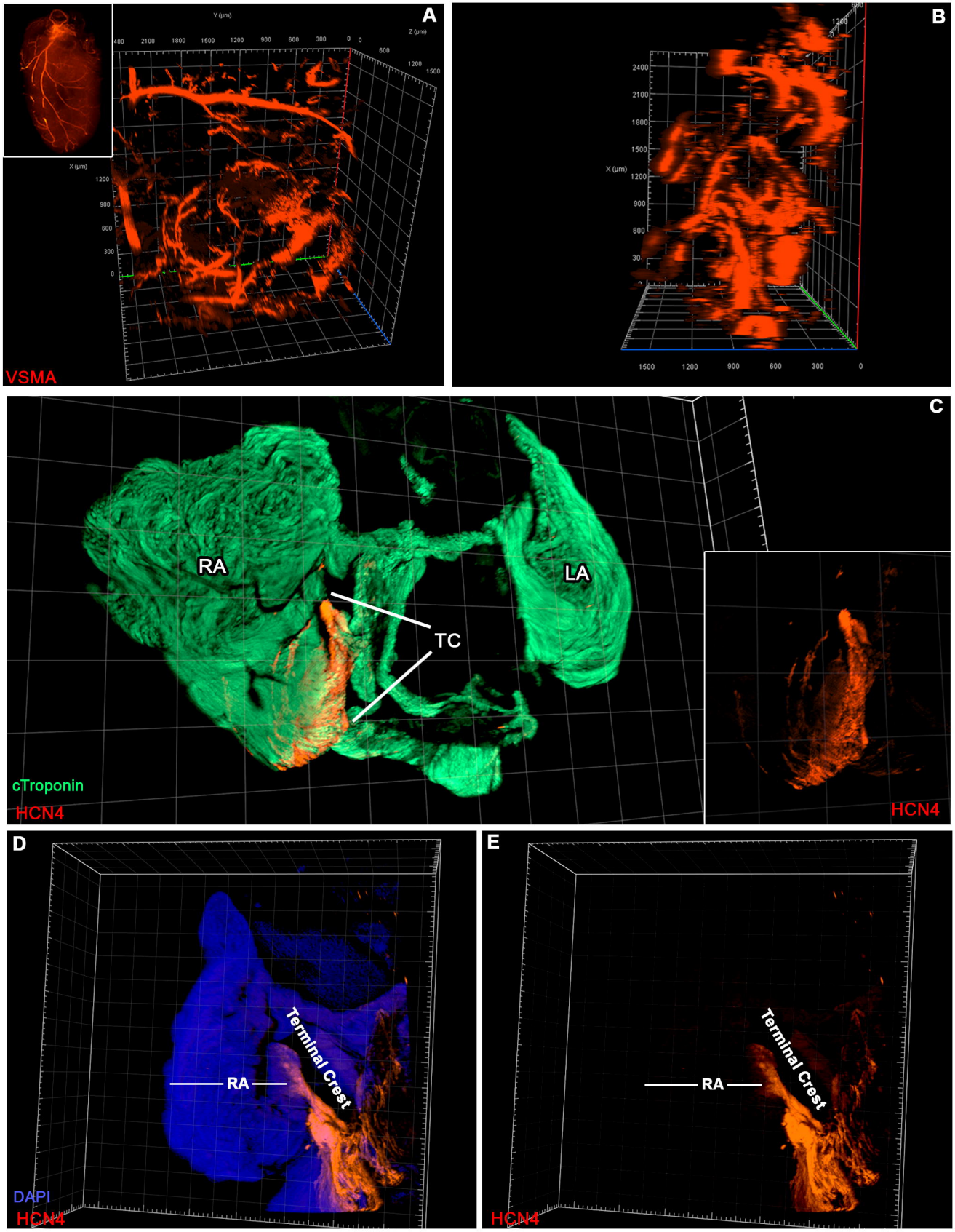
A
VSMA
B
C
RA
LA
TC
cTroponin
HCN4
HCN4
D
Terminal Crest
RA
DAPI
HCN4
E
Terminal Crest
RA
HCN4

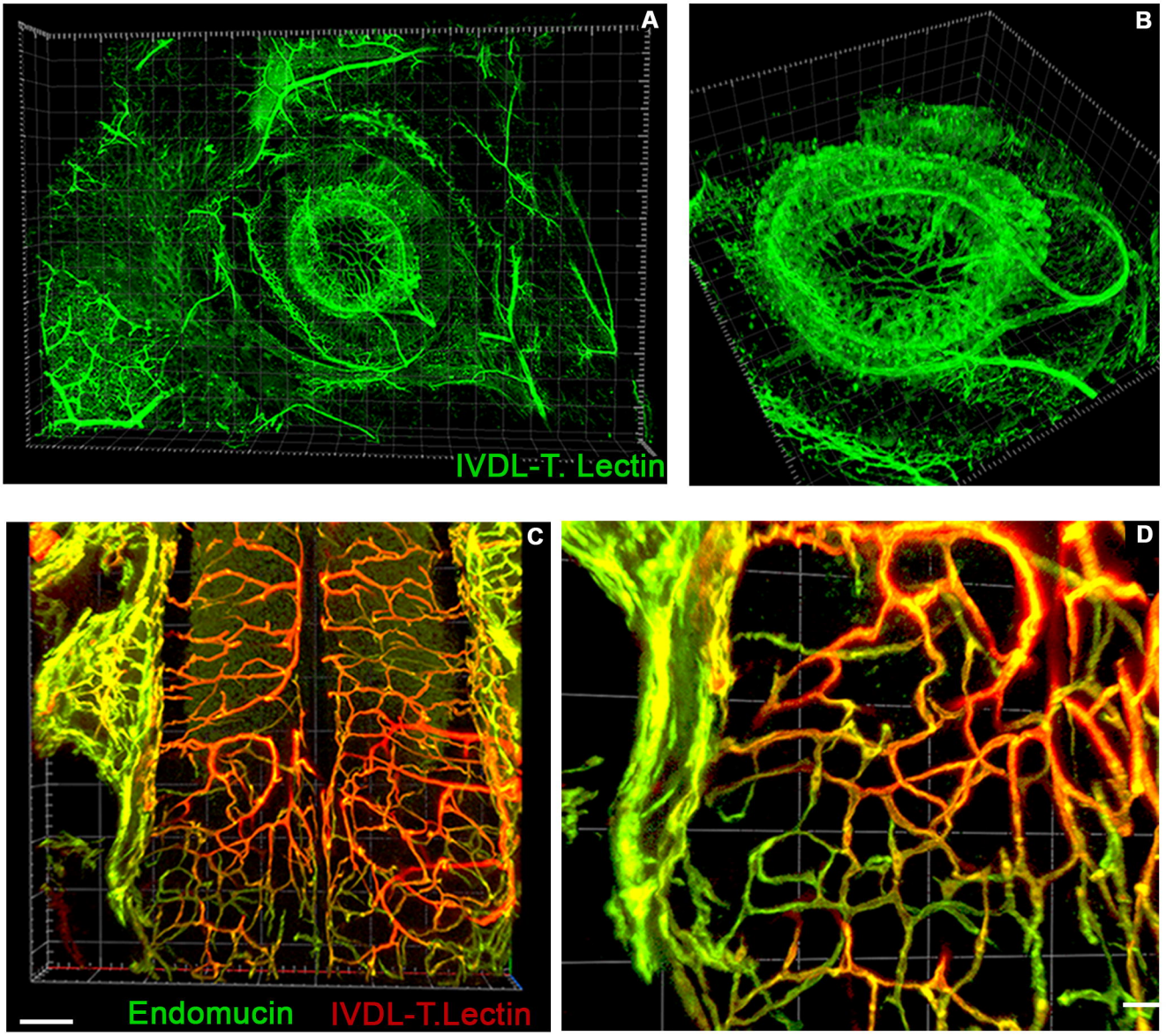
A
IVDL-T. Lectin
B
C
Endomucin
IVDL-T.Lectin
D

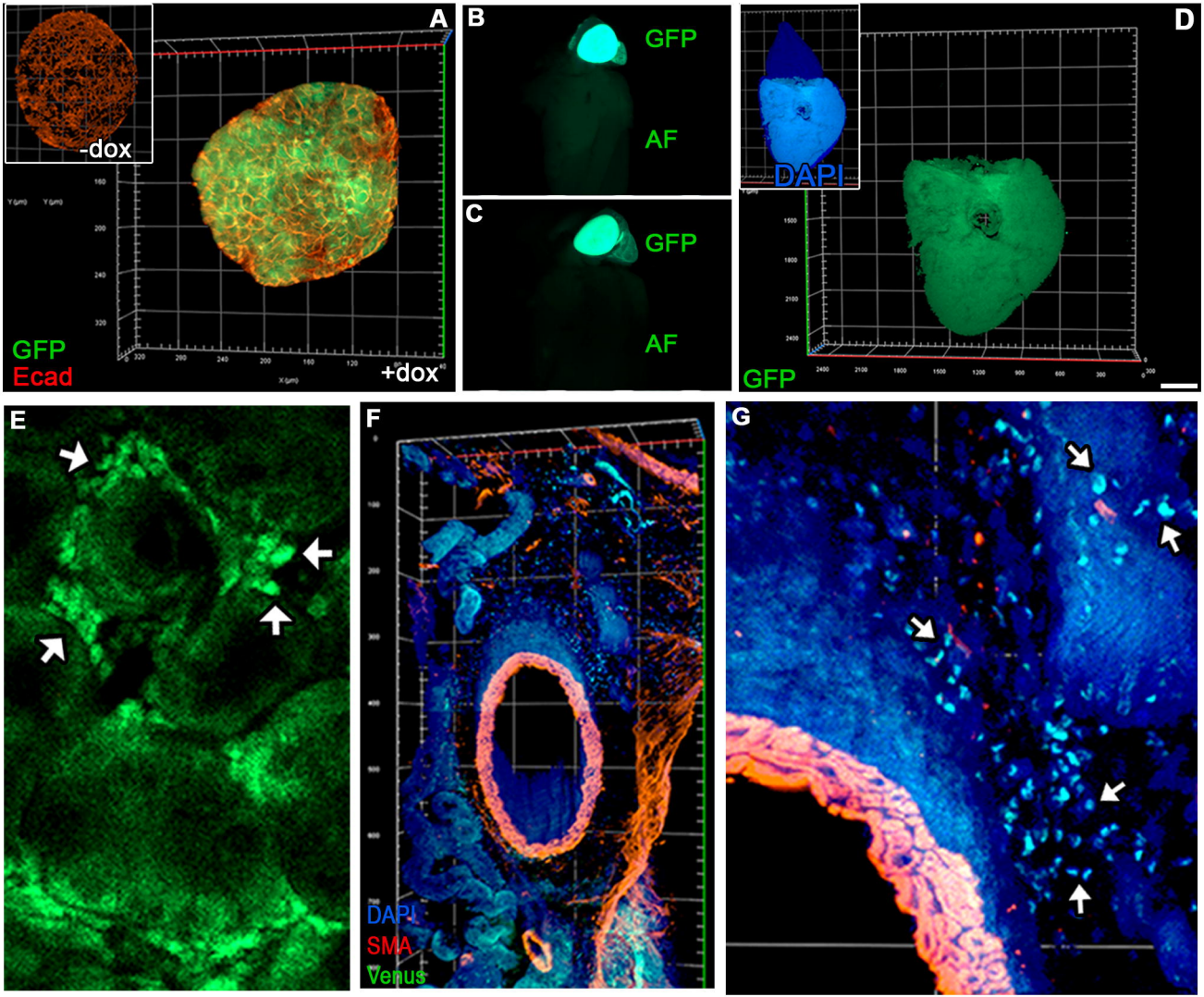
A
-dox
+dox
GFP
Ecad
B
GFP
AF
C
GFP
AF
D
DAPI
GFP
E
F
DAPI
SMA
Venus
G

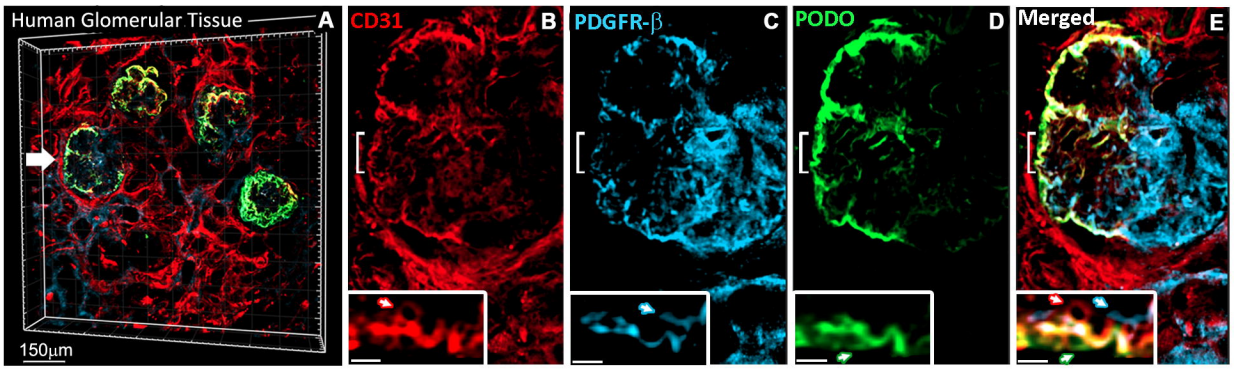
Human Glomerular Tissue
A
150µm
CD31
B
PDGFR-β
C
PODO
D
Merged
E

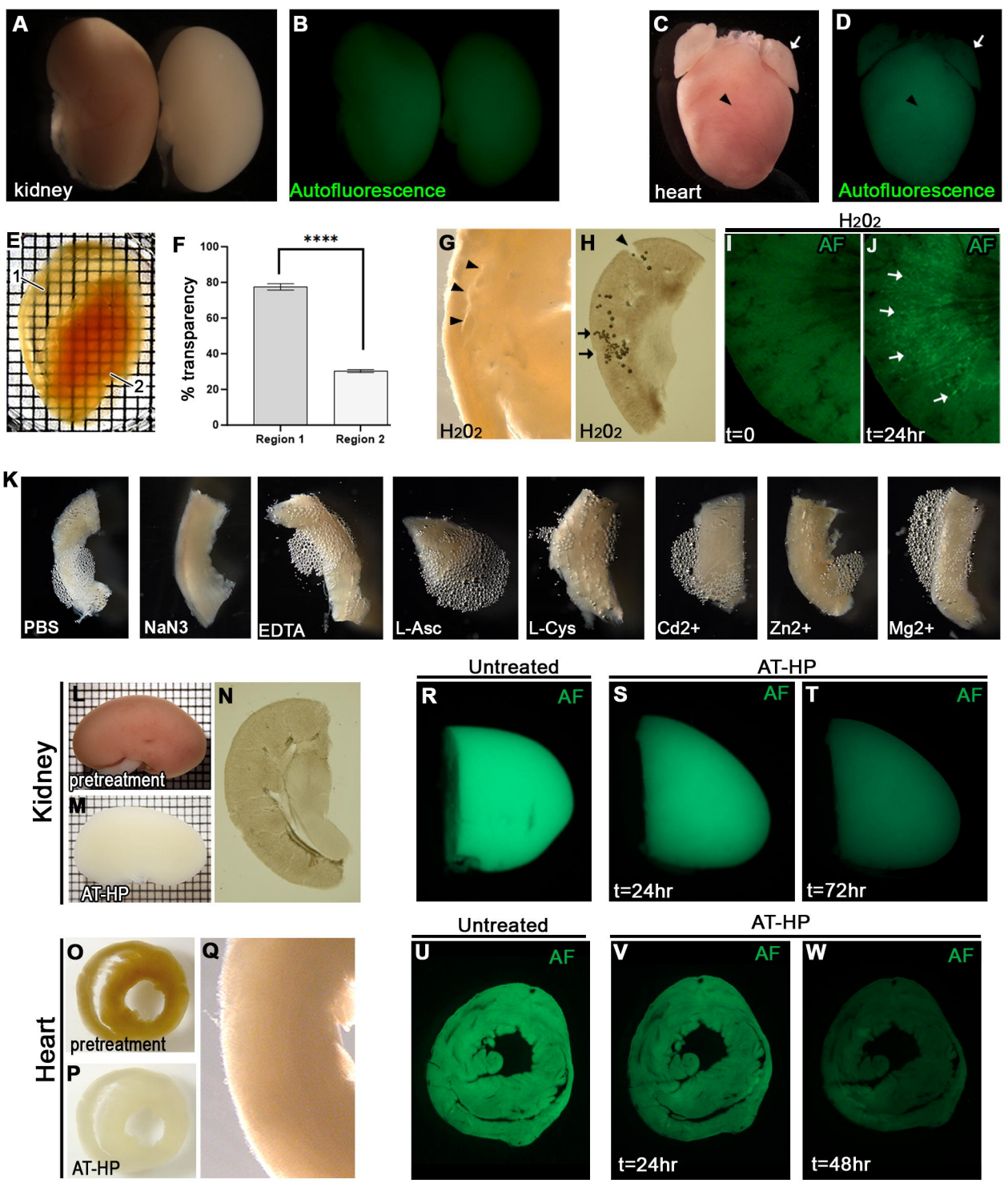
A
kidney
B
Autofluorescence
C
heart
D
Autofluorescence
E
1
2
F
****
% transparency
100
80
60
40
20
0
Region 1
Region 2
G
H2O2
H
H2O2
H2O2
I
AF
t=0
J
AF
t=24hr
K
PBS
NaN3
EDTA
L-Asc
L-Cys
Cd2+
Zn2+
Mg2+
Kidney
L
pretreatment
M
AT-HP
N
Untreated
AT-HP
R
AF
S
AF
t=24hr
T
AF
t=72hr
Heart
O
pretreatment
P
AT-HP
Q
Untreated
AT-HP
U
AF
V
AF
t=24hr
W
AF
t=48hr

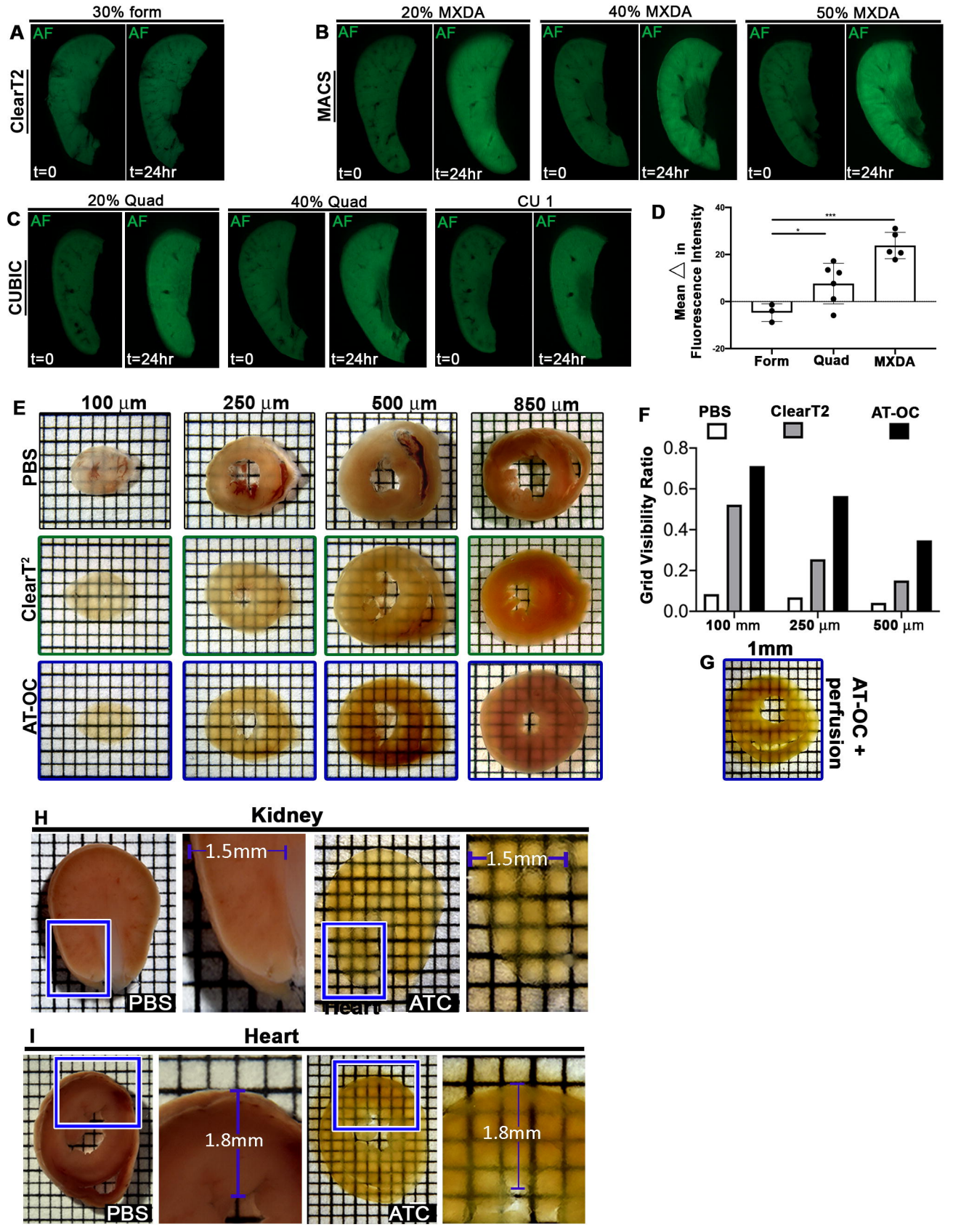
A
30% form
ClearT2
AF
t=0
t=24hr
B
20% MXDA
40% MXDA
50% MXDA
MACS
C
20% Quad
40% Quad
CU 1
CUBIC
D
Mean △ in Fluorescence Intensity
Form
Quad
MXDA
E
100 µm
250 µm
500 µm
850 µm
PBS
ClearT2
AT-OC
F
PBS
ClearT2
AT-OC
Grid Visibility Ratio
100 mm
250 µm
500 µm
G
1mm
AT-OC + perfusion
H
Kidney
1.5mm
PBS
ATC
I
Heart
1.8mm
PBS
ATC

A

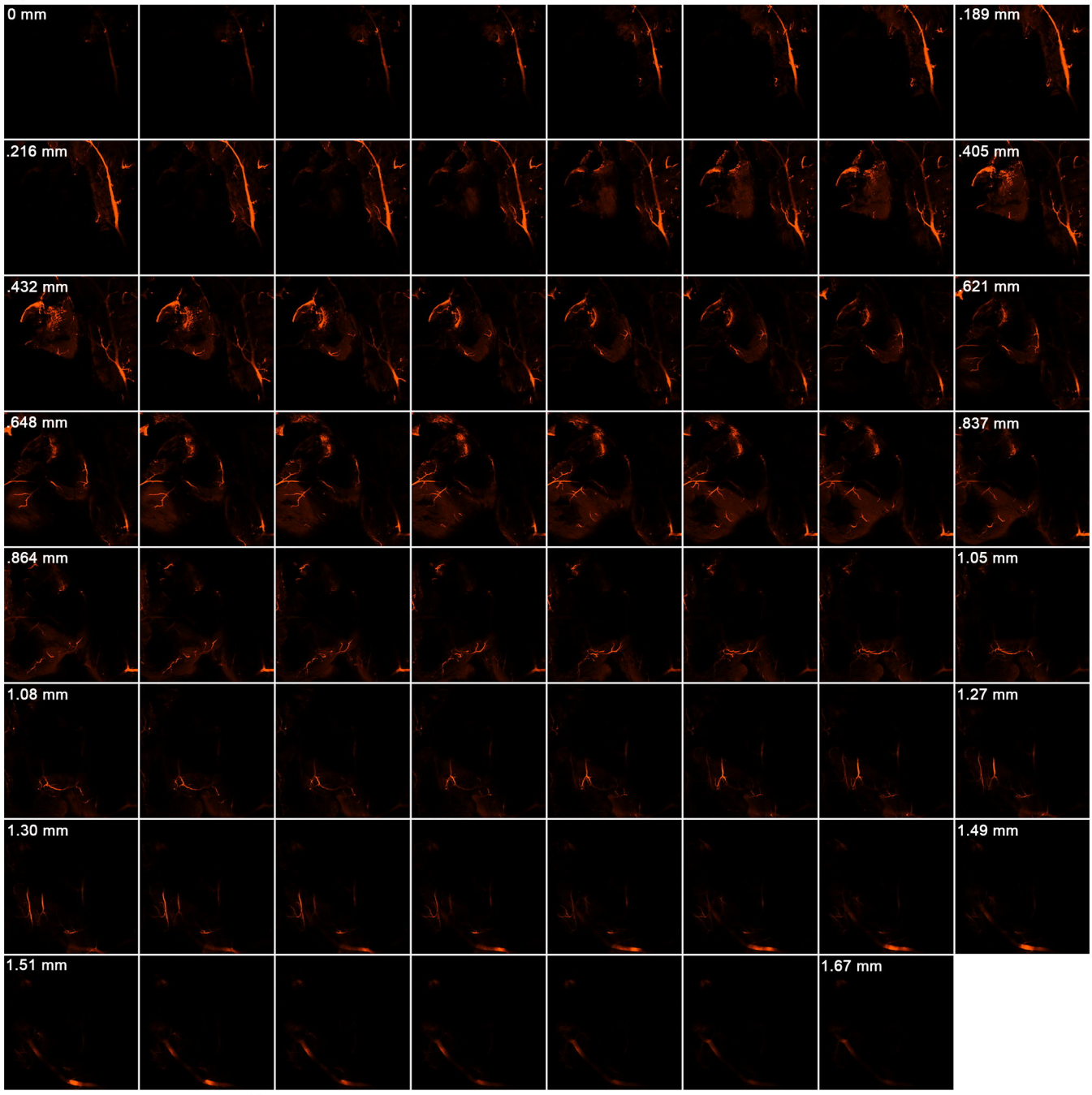
0 mm
.189 mm
.216 mm
.405 mm
.432 mm
.621 mm
.648 mm
.837 mm
.864 mm
1.05 mm
1.08 mm
1.27 mm
1.30 mm
1.49 mm
1.51 mm
1.67 mm

B

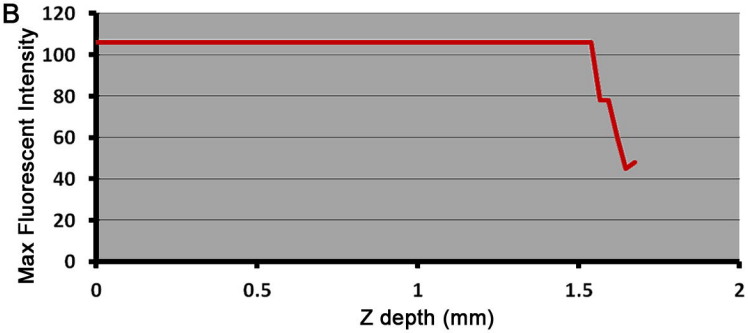
Max Fluorescent Intensity
120
100
80
60
40
20
0
0
0.5
1
1.5
2
Z depth (mm)